vehicles

MDPI

Article

Road Adhesion Coefficient Estimation Method for Distributed Drive Electric Vehicles Based on SR-UKF

Jinhui Li [1], Xinyu Wei [1,*] and Hui Peng [2]

[1] College of Vehicle and Traffic Engineering, Henan University of Science and Technology, Luoyang 471003, China; jtljh@haust.edu.cn
[2] Henan Urban Transportation Planning and Design Institute Co., Ltd., Xuchang 461001, China; hnph202511@163.com
* Correspondence: 15690768131@163.com

Abstract

To improve recognition accuracy, convergence speed, and numerical stability in estimating the road adhesion coefficient for distributed-drive electric vehicles, a nonlinear seven-degree-of-freedom vehicle dynamics model was developed based on a modified Dugoff tire model. Using the Unscented Kalman Filter (UKF) as a foundation, a Square-Root Unscented Kalman Filter (SR-UKF) algorithm was derived through covariance-square-root processing and Singular Value Decomposition (SVD). A co-simulation platform was built with CarSim and Simulink, and a vehicle speed-following model was developed for simulation analysis. The results show that the SR-UKF algorithm for road identification consistently maintains matrix positive definiteness, ensures numerical stability, speeds up convergence, and fully utilizes measurement information. Simulations under various road conditions (high-adhesion, low-adhesion, split-μ, and opposite-μ) and driving scenarios demonstrate that, compared to the traditional UKF, the SR-UKF converges faster and provides higher estimation accuracy, enabling real-time, accurate estimation of the road adhesion coefficient across multiple scenarios. Final results confirm that the SR-UKF exhibits excellent estimation accuracy and robustness on low-adhesion surfaces, confirming its superiority under high-risk conditions. This offers a dependable basis for improving vehicle active safety.

Keywords: distributed drive electric vehicles; road adhesion coefficient estimation; Square-Root Unscented Kalman Filter; CarSim-Simulink co-simulation

check for updates

Academic Editor: Julian F Dunne

Received: 11 November 2025
Revised: 4 December 2025
Accepted: 4 December 2025
Published: 6 December 2025

Citation: Li, J.; Wei, X.; Peng, H. Road Adhesion Coefficient Estimation Method for Distributed Drive Electric Vehicles Based on SR-UKF. *Vehicles* **2025**, *7*, 154. https://doi.org/10.3390/vehicles7040154

Copyright: © 2025 by the authors. Licensee MDPI, Basel, Switzerland. This article is an open access article distributed under the terms and conditions of the Creative Commons Attribution (CC BY) license (https://creativecommons.org/licenses/by/4.0/).

1. Introduction

Distributed Drive Electric Vehicles (DDEVs), characterized by their inherent advantages of independently controllable four-wheel drive forces and precisely measurable torque and rotational speed signals [1], have become a significant focus of research in vehicle engineering in recent years. Studies related to their active safety performance and handling stability are increasingly drawing academic attention [2–4]. Among these factors, road type and its adhesion conditions are key influences on vehicle dynamic behavior, making the real-time and accurate estimation of the road adhesion coefficient a crucial step in enhancing vehicle driving safety [5–8]. By dynamically identifying the road adhesion state and promptly adjusting control strategies, the handling stability of vehicles under complex operating conditions can be greatly improved. This approach has strong practical applications and is of utmost importance for developing highly reliable active safety systems [9].

Currently, road identification methods fall into two categories [10]: Cause-Based and Effect-Based methods. While Cause-Based methods have a specific predictive ability, allowing for road identification before tire-road contact, they require extra sensors, which increase costs and reduce robustness. These methods depend heavily on image quality. Conditions such as strong lighting, overcast or rainy weather, water on the road, or dirt can lower image clarity, negatively impacting the estimation of the road adhesion coefficient [11–13].

Effect-based identification methods estimate the road adhesion coefficient by analyzing vehicle state response parameters induced by changes in road conditions. These methods typically require no additional sensors and exhibit strong adaptability to operational environments, thus garnering widespread attention. Xu et al. [14] proposed a dimensionless tire model that establishes an analogy between the Burckhardt model's adhesion coefficient and the peak adhesion coefficient, thereby constructing a relationship between tire mechanical characteristics and the peak adhesion coefficient, and employing the UKF for estimation. Huang et al. [15] proposed a low-cost multi-source fusion method for estimating road surface friction coefficients. This approach first divides input images into sky and road regions via semantic segmentation, then dynamically fuses multi-source features to enhance the robustness of the estimation effectively. However, its performance relies heavily on the accuracy of image semantic segmentation. Under extreme weather conditions, the estimation accuracy of multi-source fusion is susceptible to environmental degradation. Furthermore, the approach fails to incorporate real-time feedback from vehicle dynamics, limiting adaptability in complex scenarios. Deng et al. [16] proposed an Interactive Multiple Model Adaptive UKF (IMM-AUKF) for four-wheel-drive vehicles, enhancing estimation accuracy and convergence speed by switching observers for different conditions. Nevertheless, the multi-model switching mechanism increases algorithmic complexity and fails to effectively address the numerical singularity in the covariance matrix, thereby affecting numerical stability. Ge et al. [17] proposed a square-root volume Kalman filtering algorithm incorporating a maximum correlation entropy criterion, establishing a seven-degree-of-freedom nonlinear distributed-drive vehicle dynamics model. This algorithm enables precise estimation of vehicle longitudinal velocity, lateral velocity, yaw rate, and wheel rotational angular velocity based on low-cost sensor signals. However, the method incurs a significant computational burden and exhibits noticeable estimation delays under dynamic operating conditions. Wang et al. [18], addressing the insufficient time-varying road-tracking capability of traditional UKF, proposed a Fuzzy Forgetting Factor UKF that achieves rapid response to sudden road condition changes, albeit potentially at the cost of steady-state estimation accuracy. Yang et al. [19] classified road types and designed a State-Constrained Square-Root Cubature Kalman Filter (SR-CKF) for estimation. While this improved identification robustness, SR-CKF has limited capability in characterizing probability distributions for highly nonlinear systems, leaving room for improvement in estimation accuracy and flexibility. Liu et al. [20] addressed the insufficient estimation accuracy and adaptive capability of traditional UKF on complex roads by proposing an Adaptive Attenuation UKF (AAUKF) algorithm. However, its mechanism for enhancing tracking capability might introduce additional estimation fluctuations in high-noise environments. Zhang et al. [21] proposed a High-Order Strong Tracking Cubature Kalman Filter (HSTCKF) algorithm that integrates high-order CKF with strong tracking theory. However, the introduced strong tracking mechanism may increase the algorithm's computational complexity. Chen et al. [22] proposed a joint estimation algorithm for the driving state and the road surface adhesion coefficient of four-wheel independent-drive electric vehicles, based on federated Kalman filtering and an intelligent bionic antlion optimization algorithm. However, its complex architecture, which integrates multiple algorithms, increases the computational burden, leaving room for optimization to improve real-time adaptability

in vehicle-embedded systems and dynamic response speed under complex road conditions. The specific comparison of the above literature is shown in Table 1.

Table 1. Comparison of existing methods for estimating pavement adhesion coefficients.

Literature	Core Methodology	Existing Limitations
Xu et al. [14]	Nondimensional Tire Model + UKF	The robustness and numerical stability of the algorithm have not been discussed in depth.
Huang et al. [15]	Image semantic segmentation + multi-source feature fusion	Highly dependent on image segmentation accuracy, with performance degradation under extreme weather conditions and a lack of vehicle dynamics feedback.
Deng et al. [16]	Interactive Multi-Model Adaptive UKF	The model-switching mechanism increases algorithmic complexity without resolving the issue of numerically singular covariance matrices.
Ge et al. [17]	Square Root Volume Kalman Filter	The computational burden is heavy, with noticeable estimation lag under dynamic operating conditions.
Wang et al. [18]	Uncertain Forgetfulness Factor UKF	It may be possible to achieve a rapid response capability at the expense of steady-state estimation accuracy.
Yang et al. [19]	State-Restrained SR-CKF	The ability to characterize the probability distribution of highly nonlinear systems is limited.
Liu et al. [20]	Adaptive Decaying UKF	In environments with intense noise, additional estimation fluctuations may be introduced.
Zhang et al. [21]	High-Order Strong Tracking Volumetric Kalman Filter	The improved tracking system raises the algorithm's computational complexity.
Chen et al. [22]	Federated Kalman Filter	Multi-algorithm fusion architectures are complex, impose heavy computational loads, and need optimization for real-time performance.

Furthermore, Miguel Meléndez Useros et al. [23] proposed a static output feedback path-tracking fault-tolerant controller (SOF-FT-PTC), which addresses system nonlinearities through linear parameter transformation. In another study, Guo Jianhua et al. [24] introduced a cooperative control framework that enhances vehicle maneuvering stability by optimizing torque distribution and integrating steering-drive coordination. Both studies highlight the crucial reliance of advanced vehicle control systems on accurate, real-time state information, with the road surface adhesion coefficient serving as a key parameter that directly impacts control effectiveness. However, existing road surface adhesion estimation methods remain limited, particularly regarding the numerical stability of filtering algorithms and their ability to adapt to various transient road conditions.

To estimate the road adhesion coefficient, this paper develops an algorithm using the Square-Root Unscented Kalman Filter (SR-UKF) [25–27]. The estimation framework is based on a 7-degree-of-freedom vehicle dynamics model that includes the Dugoff tire model. The CarSim vehicle model is employed for simulation validation, creating a test environment that closely resembles real-world conditions. Additionally, a distributed drive electric vehicle model is implemented on a CarSim-Simulink co-simulation platform to verify the effectiveness and performance of the proposed SR-UKF method.

2. Vehicle Dynamics Model Development

Figure 1 shows the seven-degree-of-freedom vehicle dynamics model established herein demonstrates the relationship between the ground inertial coordinate system O−XY and the vehicle coordinate system O−XY. The origin O of the ground inertial coordinate system is fixed to the ground and independent of vehicle motion. The origin CoG of the vehicle coordinate system is rigidly fixed to the vehicle's center of mass and moves with the vehicle body. The positive directions of the longitudinal velocity v_x and lateral

velocity v_y correspond to the positive directions of the x-axis and y-axis, respectively. The yaw angular velocity r is positive when rotated around the positive z-axis (in accordance with the right-hand rule). The longitudinal force F_x acting on the tires is positive when directed towards the vehicle's forward motion; the lateral force F_y is positive when directed towards the vehicle's left side. The front wheel steering angle δ_f is positive when turning counterclockwise (left). The model's seven degrees of freedom encompass the vehicle's lateral, yaw, and roll motions, as well as the rotational motion of all four wheels.

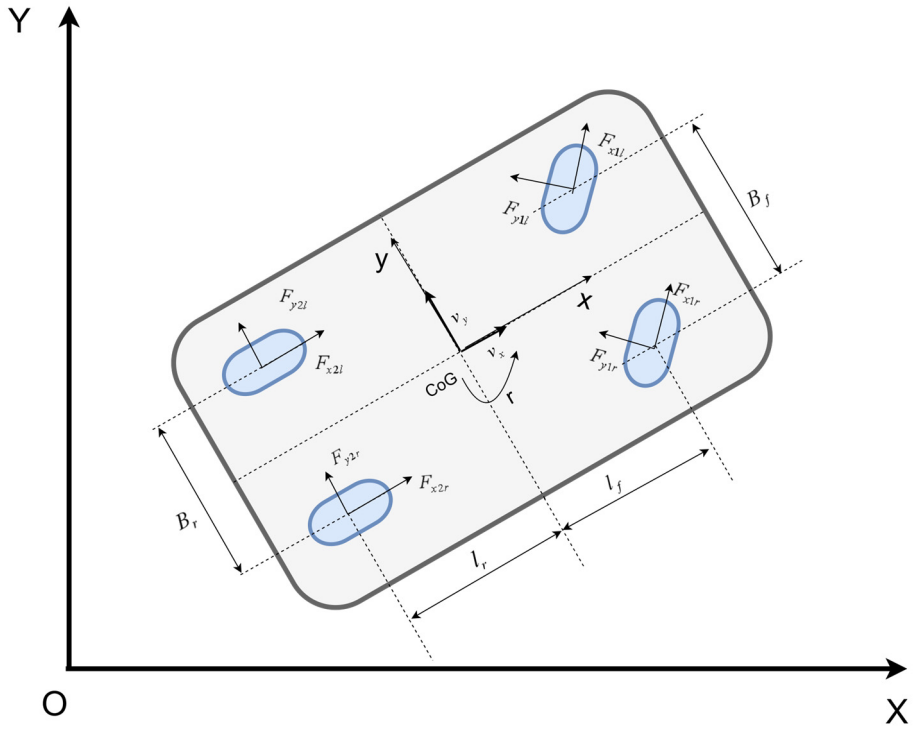

Figure 1. 7-Degree-of-freedom vehicle model.

The modeling is based on the following assumptions:

- Assuming the vehicle has a rigid body, and the origin O of the vehicle dynamics model coincides with the position of the center of mass.
- Neglecting the effects of air resistance.
- Neglecting vehicle pitch and roll motions caused by the suspension system.
- All tires share identical characteristics.
- Neglecting the influence of the suspension system on vehicle dynamics.

Furthermore, based on the aforementioned rigid-body assumption, the dynamic vertical load on each tire is calculated using a quasi-static formula. This method directly computes load transfer from the vehicle's geometric parameters and inertial forces, without relying on the suspension's dynamic characteristics. This approach ensures computational efficiency while maintaining adequate accuracy under typical driving conditions. The specific formula for vertical load is given in Equation (9).

The dynamic equations for the 7-degree-of-freedom vehicle model are as follows:

The longitudinal dynamic equation is as follows:

$$\dot{v}_x = \frac{1}{m}[(F_{x1l} + F_{x1r})\cos\delta_f - (F_{y1l} + F_{y1r})\sin\delta_f + F_{x2l} + F_{x2r}] + v_y \cdot r \tag{1}$$

The lateral dynamic equation is as follows:

$$\dot{v}_y = \frac{1}{m}[(F_{x1l} + F_{x1r})\sin\delta_f + (F_{y1l} + F_{y1r})\cos\delta_f + F_{y2l} + F_{y2r}] - v_x \cdot r \tag{2}$$

The yaw dynamics equation is as follows:

$$\begin{aligned} \dot{r} = \tfrac{1}{I_z}\{&\tfrac{B_f}{2}[(F_{x1r} - F_{x1l})\cos\delta_f + (F_{y1l} - F_{y1r})\sin\delta_f] + \\ &l_f[(F_{x1l} + F_{x1r})\sin\delta_f + (F_{y1l} + F_{y1r})\cos\delta_f] + \\ &\tfrac{B_r}{2}(F_{x2r} - F_{x2l}) - l_r(F_{y2l} + F_{y2r})\} \end{aligned} \tag{3}$$

The rotational equation of the wheel is as follows:

$$I_w\dot{\omega}_i = T_{ij} - R \cdot F_{xi} \tag{4}$$

In the formula, I_z is the moment of inertia of the vehicle about the z-axis; a_x is the longitudinal acceleration; a_y is the lateral acceleration; r is the yaw angular velocity; l_f, l_r represent the distances from the vehicle's center of gravity to the front and rear axles, respectively; B_f, B_r represent the wheelbase of the front and rear axles, respectively; δ_f is the front wheel steering angle input; subscript 1l, 1r, 2l, 2r represent the left front wheel, right front wheel, left rear wheel, and right rear wheel, respectively; m represents the curb weight of the vehicle; F_x is the longitudinal force on the wheel; F_y represents the lateral force on the wheel; ω_i is the wheel speed; I_w is the rotational inertia of the wheel about its axis; the subscript i denotes the i-th wheel (i = 1l, 1r, 2l, 2r); T_{ij} denotes wheel torque, positive for drive, negative for braking; R is the rolling radius of the wheel. The paper establishes a geometric relationship between hub velocity and wheel speed using rolling radius, without explicitly modeling tire vertical deformation.

This study uses the Dugoff tire model due to its algorithmic compatibility and computational benefits. The model explicitly includes the road adhesion coefficient as a key parameter, providing a clear structure suitable for state estimation with filters like the SR-UKF. Compared to the more computationally demanding Magic Formula model, which requires many parameters, the Dugoff model offers a simpler approach with lower computational cost. This efficiency is essential for meeting the real-time control needs of distributed-drive electric vehicles. The mechanical relationships within the model are shown in Figure 2.

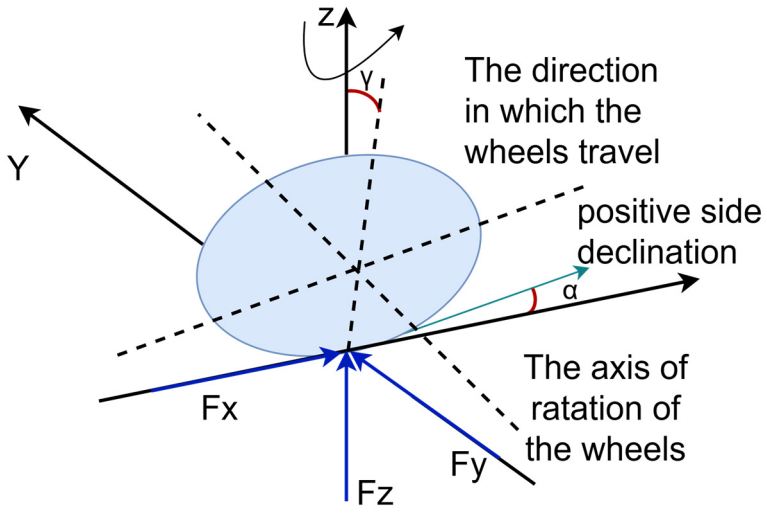

Figure 2. Dugoff tire model.

The following formula gives the actual longitudinal and lateral forces on a tire:

$$F_{xij} = \mu_{ij} F_{xij}^0 = \mu_{ij} F_{z_ij} C_x \frac{\lambda_{ij}}{1-\lambda_{ij}} f(L) \tag{5}$$

$$F_{yij} = \mu_{ij} F_{yij}^0 = \mu_{ij} F_{z_ij} C_y \frac{\tan(\alpha_{ij})}{1-\lambda_{ij}} f(L) \tag{6}$$

In particular, the function $f(L)$ determines the saturation characteristics of the tire force:

$$f(L) = \begin{cases} 1 & L \geq 1 \quad (\text{Linear region}) \\ L(2-L), & L < 1 \quad (\text{Non-linear saturation region}) \end{cases} \tag{7}$$

The formula for calculating the key parameter L is as follows:

$$L = \frac{(1-\lambda_{ij})(1-\varepsilon v_x \sqrt{C_x^2 \lambda_{ij}^2 + C_y^2 \tan^2 \alpha_{ij}})}{2\sqrt{C_x^2 \lambda_{ij}^2 + C_y^2 \tan^2 \alpha_{ij}}} \tag{8}$$

This model precisely controls the nonlinear transition of tire forces from linear to saturated states via the parameter L. When $L \geq 1$, the system operates within the linear range, where tire force F_{xij}^0 and the tire force ratio F_{yij}^0 exhibit only linear or quasi-linear relationships with slip ratio, yaw angle, and stiffness, remaining consistently below the road surface adhesion limit. Upon entering the nonlinear saturation regime where $L < 1$, the force saturation function $f(L)$ takes effect, constraining tire forces within the physical upper limit determined by μ·Fz. As slip intensifies and L decreases further, $f(L)$ exhibits nonlinear decay, thereby accurately simulating the saturation and decay characteristics of tire forces.

In the formula, μ_{ij} is the road surface adhesion coefficient for each wheel, F_{yij}^0 represent the normalized longitudinal and lateral tire forces for each wheel (where i = 1, 2 denotes front and rear wheels, respectively, and j = l, r denotes left and right wheels, respectively); C_x, C_y indicate the force per unit slip and cornering stiffness of the tire, respectively, with these parameters being specified by concrete numerical values [28], respectively; $f(L)$ is the tire model correction coefficient. When L < 1, the tire is in the nonlinear region; when L ≥ 1, it is in the linear region. ε is the velocity influence factor; λ, α represents the tire slip ratio and lateral slip angle; F_{zij} represents the vertical load on each tire.

Then, the vertical load on the wheel is as follows:

$$\begin{cases} F_{z1l} = \dfrac{mgl_r}{2L} - \dfrac{ma_x h_g}{2L} + \dfrac{ma_y h_g l_r}{LB_f} \\ F_{z1r} = \dfrac{mgl_r}{2L} - \dfrac{ma_x h_g}{2L} - \dfrac{ma_y h_g l_r}{LB_f} \\ F_{z2l} = \dfrac{mgl_r}{2L} + \dfrac{ma_x h_g}{2L} - \dfrac{ma_y h_g l_f}{LB_r} \\ F_{z2r} = \dfrac{mgl_r}{2L} + \dfrac{ma_x h_g}{2L} + \dfrac{ma_y h_g l_f}{LB_r} \end{cases} \tag{9}$$

In the formula, $L = l_f + l_r$, l_f, l_r represent the distances from the vehicle's center of gravity to the front and rear axles, respectively; h_g is the height of the center of mass.

Wheel center speed is as follows:

$$\begin{cases} v_{c1l} = (v_x + B_f\omega_{1l}/2)\cos\delta + (v_y + l_f\omega_{1l})\sin\delta_f \\ v_{c1r} = (v_x - B_f\omega_{1r}/2)\cos\delta + (v_y + l_f\omega_{1r})\sin\delta_f \\ v_{c2l} = v_x + B_f\omega_{2l}/2 \\ v_{c2r} = v_x - B_f\omega_{2r}/2 \end{cases} \tag{10}$$

In the formula, $v_{c1l}, v_{c1r}, v_{c2l}, v_{c2l}$ represent the speeds at the centers of the left front wheel, right front wheel, left rear wheel, and right rear wheel, respectively; $\omega_{1l}, \omega_{1r}, \omega_{2l}, \omega_{2r}$ represent the angular velocities of the left front wheel, right front wheel, left rear wheel, and right rear wheel, respectively.

The formula for calculating the slip rate is as follows:

$$\lambda_{ij} = \frac{(\omega_{ij}R - v_x)}{\max(|\omega_{ij}R|, |v_x|)} \tag{11}$$

The tire slip angles are as follows:

$$\begin{cases} \alpha_{1l} = -\delta_f + \arctan\dfrac{v_y + l_f\omega_{1l}}{v_x + B_f\omega_{1l}/2} \\ \alpha_{1r} = -\delta_f + \arctan\dfrac{v_y + l_f\omega_{1r}}{v_x - B_f\omega_{1r}/2} \\ \alpha_{2l} = \arctan\dfrac{v_y - l_r\omega_{2l}}{v_x + B_r\omega_{2l}/2} \\ \alpha_{2r} = \arctan\dfrac{v_y - l_r\omega_{2r}}{v_x - B_r\omega_{2r}/2} \end{cases} \tag{12}$$

3. Estimation of Pavement Skid Resistance Using an SR-UKF

Standard methods for estimating road surface friction coefficients include the Extended Kalman Filter (EKF) and the Unscented Kalman Filter (UKF). The EKF depends on a local linearization approximation, which makes it difficult to apply to highly nonlinear systems. Additionally, calculating the Jacobian matrix is computationally demanding and can be error-prone. UKF computations are also intensive, offer limited real-time performance in high-dimensional systems, require complex parameter tuning, and can encounter numerical singularities in the covariance matrix under high-dimensional conditions [29]. Building on the UKF framework, this paper introduces the SR-UKF method for estimating road surface friction coefficients. It does so by directly propagating and updating the square root of the covariance matrix, using numerically stable techniques like SVD. This method keeps the covariance matrix positive definite, effectively preventing numerical singularities common in high-dimensional scenarios with traditional UKFs, while also reducing computational load.

3.1. UKF Pavement Skid Resistance Estimation Method

The estimation of UKF road surface adhesion coefficients can be described as a nonlinear state-space model incorporating Gaussian white noise:

$$\begin{cases} \dot{x}(t) = f[x(t), u(t)] + w(t) \\ z(t) = h[x(t), u(t)] + v(t) \end{cases} \tag{13}$$

Among them $x(t)$ is the state vector; $u(t)$ is the input vector; $w(t) \sim N(0, Q)$ represents process noise; $v(t) \sim N(0, R)$ is the noise measurement; $f(\cdot)$ is the nonlinear state function of the system; $h(\cdot)$ is the nonlinear measurement function of the system.

During the estimation process, the target is the road adhesion coefficient of the four wheels of the distributed-drive electric vehicle. The state variables are defined as follows: $x = (\mu_{1l}, \mu_{1r}, \mu_{2l}, \mu_{2r})^T$. Select motion signals directly obtainable from onboard sensors as the observation vector, defining the observation vector as $z = (a_x, a_y, \gamma)$, where a_x, a_y represent longitudinal and lateral acceleration, respectively, and γ represents yaw angular velocity.

Let the sampling time be Δt. After discretizing the continuous-system model, we obtain the discrete state equations and observation equations under distributed input conditions:

$$x(k+1) = \begin{bmatrix} 1 & 0 & 0 & 0 \\ 0 & 1 & 0 & 0 \\ 0 & 0 & 1 & 0 \\ 0 & 0 & 0 & 1 \end{bmatrix} \begin{bmatrix} \mu_{1l} \\ \mu_{1r} \\ \mu_{2l} \\ \mu_{2r} \end{bmatrix} + w(k) \tag{14}$$

$$z(k) = \begin{bmatrix} \dfrac{F_{x1l}^0 \cos\delta - F_{y1l}^0 \sin\delta}{m} & \dfrac{F_{x1r}^0 \cos\delta - F_{y1r}^0 \sin\delta}{m} & \dfrac{F_{x2l}^0}{m} & \dfrac{F_{x2r}^0}{m} \\ \dfrac{F_{x1l}^0 \sin\delta + F_{y1l}^0 \cos\delta}{m} & \dfrac{F_{x1r}^0 \sin\delta + F_{y1r}^0 \cos\delta}{m} & \dfrac{F_{y2l}^0}{m} & \dfrac{F_{y2r}^0}{m} \\ h(3,1) & h(3,2) & h(3,3) & h(3,4) \end{bmatrix} \begin{bmatrix} \mu_{1l} \\ \mu_{1r} \\ \mu_{2l} \\ \mu_{2r} \end{bmatrix} + v(k) \tag{15}$$

In the formula, $h(3,1), h(3,2), h(3,3), h(3,4)$ respectively:

$$h(3,1) = \frac{(F_{x1l}^0 \sin\delta + F_{y1l}^0 \cos\delta) l_f - (F_{x1l}^0 \cos\delta - F_{y1l}^0 \sin\delta) B_f/2}{I_z} \tag{16}$$

$$h(3,2) = \frac{(F_{x1r}^0 \sin\delta + F_{y1r}^0 \cos\delta) l_f + (F_{x1r}^0 \cos\delta - F_{y1r}^0 \sin\delta) B_f/2}{I_z} \tag{17}$$

$$h(3,3) = \frac{-F_{y2l}^0 l_r - F_{x2l}^0 B_r/2}{I_z} \tag{18}$$

$$h(3,4) = \frac{-F_{y2r}^0 l_r + F_{x2r}^0 B_r/2}{I_z} \tag{19}$$

Additionally, the UKF algorithm generates sigma points through the U-T transformation to represent the probability distribution of state variables. These sigma points are processed through a nonlinear transformation and weighted reconstruction to perform state estimation. By incorporating the vehicle's distributed drive characteristics with the Dugoff tire model, the state estimation process includes the following steps:

1. System Initialization

$$\begin{cases} \hat{x}_0 = E(x_0) \\ P_0 = E[(x_0 - \hat{x}_0)(x_0 - \hat{x}_0)^T] \end{cases} \tag{20}$$

2. Sigma Point Generation and Weight Calculation

For a 4-dimensional state vector (n = 4), generate 2n + 1 Sigma points based on the current state mean $\hat{x}_{k|k}$ and covariance matrix $P_{k|k}$, covering the probability distribution of the state:

$$X_{k|k}^{i} = \begin{cases} \hat{x}_{k|k} & i = 0 \\ \hat{x}_{k|k} + \left(\left((n+\lambda)P_{k|k}\right)^{1/2}\right)_{i} & i = 1, 2, 3, \ldots, n \\ \hat{x}_{k|k} - \left(\left((n+\lambda)P_{k|k}\right)^{1/2}\right)_{i-n} & i = n+1, n+2, \ldots, 2n \end{cases} \tag{21}$$

In the formula, $\lambda = \alpha^2(n+k) - n$ is the scaling parameter, α is the scaling factor, β is the distribution factor, and k is the secondary distribution factor.

$$\begin{cases} w_m^{(0)} = \dfrac{\lambda}{n+\lambda} \\ w_c^{(0)} = \dfrac{\lambda}{n+\lambda} + (1 - \alpha^2 + \beta) \\ w_m^{(i)} = w_c^{(i)} = \dfrac{1}{2(n+\lambda)} \; i = 1, 2, \ldots, 2n \end{cases} \tag{22}$$

In the formula, $w_m^{(\mathrm{i})}$ and $w_c^{(\mathrm{i})}$ represent the system mean weight and covariance weight, respectively.

3. Time Updated

Sigma Point Transfer:

$$X_{k+1|k}^{i} = f(X_{k|k}^{i}, u(k)) \tag{23}$$

Prior state mean:

$$\hat{x}_{k+1|k} = \sum_{i=0}^{2n} w_m^{(i)} X_{k+1|k}^{i} \tag{24}$$

Prior covariance:

$$P_{k+1|k} = \sum_{i=0}^{2n} w_c^{(i)} (X_{k+1|k}^{i} - \hat{x}_{k+1|k})(X_{k+1|k}^{i} - \hat{x}_{k+1|k})^{T} + Q \tag{25}$$

4. Measurement Update

Observation of Sigma Point Transmission:

$$Z_{k+1|k}^{i} = h(X_{k+1|k}^{i}, u(k+1)) \tag{26}$$

Predicted Observed Mean:

$$\hat{z}_{k+1|k} = \sum_{i=0}^{2n} w_m^{(i)} Z_{k+1|k}^{i} \tag{27}$$

Calculation of Observed Covariance:

$$P_{zz,k+1} = \sum_{i=0}^{2n} w_c^{(i)} (Z_{k+1|k}^{i} - \hat{z}_{k+1|k})(Z_{k+1|k}^{i} - \hat{z}_{k+1|k})^{T} + R \tag{28}$$

Mutual covariance calculation:

$$P_{xz,k+1} = \sum_{i=0}^{2n} w_c^{(i)} (X_{k+1|k}^{i} - \hat{x}_{k+1|k})(Z_{k+1|k}^{i} - \hat{z}_{k+1|k})^{T} \tag{29}$$

Kalman Gain Calculation:

$$K_{k+1} = P_{xz,k+1} P_{zz,k+1}^{-1} \tag{30}$$

Posterior Mean Update:

$$\hat{x}_{k+1|k+1} = \hat{x}_{k+1|k} + K_{k+1}(z(k+1) - \hat{z}_{k+1|k}) \tag{31}$$

Posterior Covariance Update:

$$P_{k+1|k+1} = P_{k+1|k} - K_{k+1}P_{zz,k+1}K_{k+1}^T \tag{32}$$

In the equation, X represents the state sigma point, x represents the estimated mean of the state vector, Z represents the measurement sigma point, and z represents the predicted measurement mean.

3.2. SR-UKF Road Surface Friction Coefficient Estimation

To further improve the accuracy and robustness of the UKF, enhancements were made, resulting in the development of the Square Root Unscented Kalman Filter (SR-UKF) [30,31]. The process is shown in Figure 3, with the following key improvements applied to the estimator:

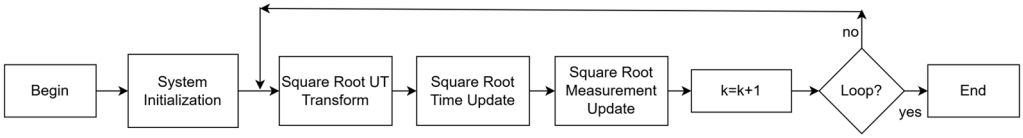

Figure 3. Flowchart of the SR-UKF algorithm.

1. Simplification of Low-Dimensional Matrix Operations

When generating Sigma points and updating the covariance matrix in UKF, frequent matrix square root operations are required on the full-rank covariance matrix P. If the state dimension n is large, the computational complexity of Cholesky decomposition is $O(n^3)$, and it is prone to failure when P is close to singular. The SR-UKF leverages the low-rank structure of the covariance square root matrix S, transforming high-dimensional matrix operations on P into low-dimensional column vector-level operations on S:

$$X_{k|k}^i = \begin{cases} \hat{x}_{k|k} & i = 0 \\ (\hat{x}_{k|k} + \sqrt{n+\lambda} \cdot S_{k|k})_i & i = 1, 2, 3, \ldots, n \\ (\hat{x}_{k|k} - \sqrt{n+\lambda} \cdot S_{k|k})_{i-n} & i = n+1, n+2, \ldots, 2n \end{cases} \tag{33}$$

2. Ensuring Positive Definiteness of the Covariance Matrix

Traditional UKF filtering directly stores and updates the covariance matrix P_k. This covariance matrix may become non-positive definite due to rounding, truncation, or modeling errors, compromising the filter's convergence and potentially leading to divergent estimation results. To this end, the SR-UKF algorithm replaces the original covariance matrix with its square root form, i.e., by using $P_k = S_k S_k^T$ to consistently maintain S_k as positive definite. The specific algorithm is as follows:

Calculate the square root of the initial covariance matrix:

$$S_0 = chol(P_0) \tag{34}$$

Perform singular value decomposition (SVD) on the covariance matrix:

$$P_{k+1|k} = UDV^T \tag{35}$$

$$D = \max(D, \varepsilon I) \tag{36}$$

$$S_{k+1|k} = U\sqrt{D}V^T \tag{37}$$

Calculation of the Square Root of the Observed Covariance:

$$P_{zz|k+1} = UDV^T \tag{38}$$

$$D = \max(D, \varepsilon I) \tag{39}$$

$$S_{zz|k+1} = U\sqrt{D}V^T \tag{40}$$

Square root of posterior covariance update:

$$P_{k+1|k+1} = UDV^T \tag{41}$$

$$D = \max(D, \varepsilon I) \tag{42}$$

$$S_{k+1|k+1} = U\sqrt{D}V^T \tag{43}$$

To avoid numerical ill-posedness, we enforce non-negativity of singular values by setting $\varepsilon = 10^{-6}$, where U, V are orthogonal matrices, and $D = diag(\sigma_1, \sigma_2, \ldots, \sigma_n)$ is the singular value diagonal matrix. The improved approach directly replaces operations on the P matrix with the square root matrix S, mechanically ensuring the semi-positive definiteness of the covariance matrix. This fundamentally resolves the filtering instability and divergence issues caused by non-positive-definiteness in UKFs, thereby enhancing the algorithm's reliability during prolonged iterations and in high-noise scenarios.

3. Calculation of Kalman Gain Based on SVD

When calculating the Kalman gain $K_{k+1} = P_{xz,k+1}P_{zz,k+1}^{-1}$ in the UKF, if the measurement covariance P_{zz} approaches the singularity, numerical instability may occur during matrix inversion. The SR-UKF similarly employs SVD on the measurement covariance P_{zz} to generate the square root S_{zz}, and rewrites the gain calculation as follows:

$$K_{k+1} = P_{xz,k+1}(S_{zz,k+1}S_{zz,k+1}^T)^{-1} \tag{44}$$

$$K_{k+1} = P_{xz,k+1}S_{zz,k+1}^{-T}S_{zz,k+1}^{-1} \tag{45}$$

The parameters for the SR-UKF algorithm employed in this study were determined through a systematic approach, with the following specific settings: the process noise covariance matrix Q was configured based on the time-varying characteristics of the state variables. Considering the slow variation in the road surface friction coefficient μ over the sampling period, a slight noise variance $Q = 0.1I_4$ was assigned, balancing state tracking capability with noise suppression requirements. The measurement noise covariance matrix R was set to $R = 0.1I_3$ based on the typical measurement accuracy of reference sensors, reasonably reflecting the uncertainty of different observations. Due to inherent uncertainty in the initial state, the initial error covariance matrix was set to $P_0 = 10^{-3}I_4$, enabling the filter to correct estimates during the initial phase rapidly. The parameter values for the unscented transform follow standard recommendations, with scaling parameters set to α = 0.001, k = 0, and $\beta = 2$. This configuration ensures the Sigma point set effectively characterizes the probabilistic distribution properties of the state.

4. Simulation Analysis and Verification

4.1. Matlab/Simulink and CarSim Joint Simulation Modeling

To validate the efficacy and performance enhancement of the SR-UKF algorithm, this paper selects the standard UKF as the core comparative benchmark. This choice is based on

the following considerations: as a numerically stable variant of the UKF, the SR-UKF shares the same algorithmic framework as the standard UKF. Direct comparison can effectively isolate and highlight the contributions of both the square-root covariance treatment and SVD to improving numerical stability, accelerating convergence, and enhancing accuracy. The primary focus of this paper is on strengthening the numerical robustness of the state estimator rather than designing adaptive noise or complex multi-model structures. Therefore, comparison with the UKF, which shares the same fixed noise assumption, is most appropriate. Based on this, a joint simulation platform integrating CarSim and Simulink was established. The overall architecture is shown in Figure 4, and the vehicle parameters are detailed in Table 2.

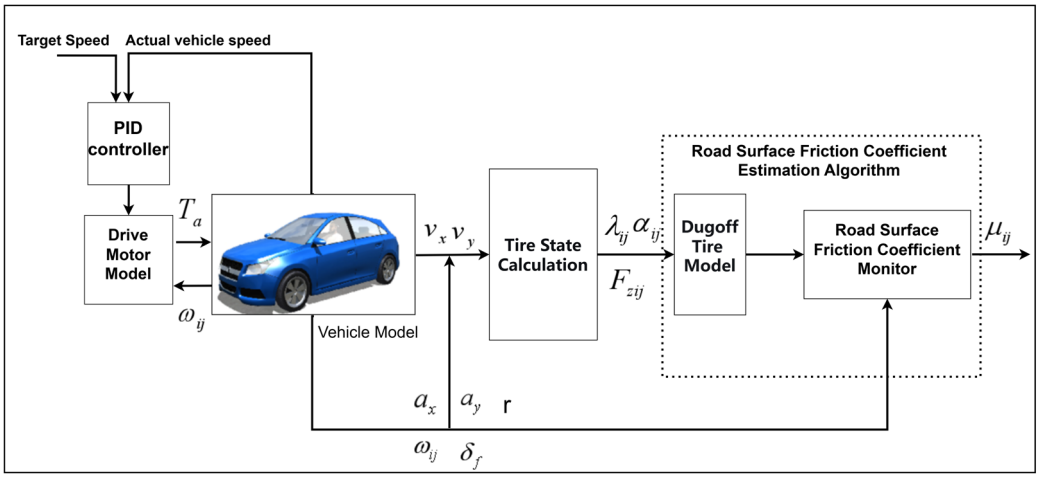

Figure 4. Integrated simulation framework architecture.

Table 2. Simulation vehicle parameter values.

Parameters	Numerical Value
Gross Vehicle Weight/kg	1765
Distance from the center of gravity to the front axle/m	1.204
Distance from the center of gravity to the rear axle/m	1.396
Center of mass height above ground/m	0.500
Whole vehicle *Z*-axis rotational inertia (kg m^2)	2700
Wheel rolling radius/m	0.354
Front axle track width/m	1.600
Rear axle track width/m	1.600
Tire Rotational Inertia/(kg m^2)	0.9
Force per unit slip/N	89,700
Cornering stiffness (N/rad)	85,300

Model mismatch in simulation is achieved through the following configuration: the CarSim high-fidelity vehicle model employs a magic formula tire model, whilst the observer is based on a simplified Dugoff model. This structural and parametric inherent discrepancy effectively replicates the model uncertainty present in real-world systems. The final results demonstrate that the SR-UKF algorithm maintains high estimation accuracy under these mismatched conditions, proving its exceptional robustness and potential for practical deployment.

In Figure 4, the drive motor model is a permanent-magnet synchronous motor, a nonlinear, time-varying, strongly coupled complex system. Before modeling, the following assumptions are made:

1. Neglecting motor core saturation, eddy current, and hysteresis losses;
2. The stator's three-phase windings are connected in a Y configuration and symmetrically distributed, with their axes offset by 120°;
3. The induced electromotive force generated by the three-phase stator armature windings of the motor is a sine wave.

To simplify the nonlinear characteristics of three-phase AC motors, the Park transformation is employed to convert the three-phase stationary coordinate system (abc) into a two-phase rotating coordinate system (d-q), thereby establishing a linearized model. The core equations are as follows:

The voltage equation is as follows:

$$\begin{cases} u_d = R_s i_d + L_d \dfrac{di_d}{d_t} - \omega_e L_q i_q \\ u_q = R_s i_q + L_q \dfrac{di_q}{dt} + \omega_e L_d i_d + \omega_e \psi_f \end{cases} \tag{46}$$

In the equation, u_d, u_q represent the d-axis and q-axis stator voltages, respectively; represent the d-axis and q-axis stator voltages, respectively; L_d, L_q denote the d-axis and q-axis inductances; i_d, i_q denote the d-axis and q-axis stator currents, respectively; R_s denotes the stator resistance; ω_e denotes the electrical angular velocity; and ψ_f denotes the permanent magnet flux linkage.

The electromagnetic torque equation is as follows:

$$T_e = \frac{3}{2} p_n [\psi_f i_q + (L_d - L_q) i_d i_q] \tag{47}$$

In the formula, T_e represents the electromagnetic torque (N·m), and p_n denotes the number of pole pairs in the motor.

The stator flux linkage equation is as follows:

$$\begin{cases} \psi_d = L_d i_d + \psi_f \\ \psi_q = L_q i_q \end{cases} \tag{48}$$

In the equation, ψ_d, ψ_q represent the stator flux components along the d-axis and q-axis, respectively.

The equation of mechanical motion is as follows:

$$T_e - T_L = J_m \frac{d\omega_m}{dt} + B_m \omega_m \tag{49}$$

In the equation, T_L represents the motor load torque (N·m), J_m denotes the motor rotational inertia (kg·m^2), ω_m indicates the motor mechanical angular velocity (rad/s), and B_m signifies the viscous friction coefficient (N·m·s/rad); where $\omega_e = p_n \omega_m$.

In Figure 4, the PID controller is used for vehicle speed tracking. To directly investigate the cooperative control law between speed tracking and torque distribution in distributed drive systems, the human–machine interface between driver and pedal is simplified. A hierarchical control architecture is adopted to allocate speed-following and distributed torque rationally. The upper layer controls vehicle speed via PID, generating a total desired driving torque based on the deviation between the target v_o and actual speed v_r as input. The middle layer directly generates the total driving torque through a PID controller. This torque is transmitted to each hub motor via the middle-layer distribution strategy, ultimately driving the vehicle to track the target speed.

Total Drive Torque:

$$T = K_p \cdot e(t) + K_i \cdot \int_0^t e(t)d(t) + K_d \cdot \frac{de(t)}{dt} \tag{50}$$

Speed deviation:

$$e(t) = v_o(t) - v_r(t) \tag{51}$$

In the equation, K_p, K_i, K_d denote the proportional, integral, and derivative coefficients, respectively; $e(t)$ represents the vehicle speed deviation; $v_o(t)$ denotes the target speed; and $v_r(t)$ represents the actual speed.

4.2. Simulation Verification Analysis Under Typical Operating Conditions

To evaluate the algorithm's performance, the SR-UKF algorithm's estimation results were compared with those of the traditional UKF algorithm. Four typical driving scenarios were selected for simulation: straight-line acceleration on high-friction surfaces, turning on low-friction surfaces, constant-speed straight-line driving on opposing lanes, and straight-line acceleration on opposing lanes.

Secondly, to evaluate the estimation accuracy and performance of the square root Unscented Kalman filter, this paper employs the mean absolute error as one of the evaluation metrics. The formula for calculating the mean absolute error is as follows:

$$MAE = \frac{\sum |y_i - \hat{y}_i|}{n} \; i = 1 \sim n \tag{52}$$

In the formula, n denotes the total number of data samples, y_i represents the actual value of the i-th sample, and $\hat{y}_i$ denotes the predicted value of the i-th sample.

4.2.1. Simulation of High-Adhesion Coefficient Pavement Linear Acceleration Conditions

During simulation, the road surface adhesion coefficient was set to 0.85, with an initial vehicle speed of 20 km/h, a steering wheel angle of 0°, and a throttle opening of 0.3. The simulation results are shown in Figure 5. The SR-UKF algorithm's estimated curve rapidly and accurately converges to the actual value of 0.85 within approximately 0.4 s, demonstrating a fast convergence rate. In contrast, the traditional UKF algorithm exhibits unstable estimation and fails to converge effectively throughout the simulation. In terms of estimation accuracy and robustness, as shown in Table 3, the SR-UKF exhibits a mean absolute error of merely 0.0031. Compared to the UKF's mean absolute error of 0.0430, this represents a reduction in estimation error of approximately 92.8%. This demonstrates that the SR-UKF outperforms the traditional UKF algorithm in both steady-state estimation accuracy and numerical stability.

Table 3. Mean absolute error for straight-line acceleration on high-adhesion coefficient pavement.

Wheel	UKF	SR-UKF
Left front wheel	0.0298	0.0031
Right front wheel	0.0553	0.0030
Left rear wheel	0.0289	0.0032
Rear right wheel	0.0579	0.0032
Average value	0.0298	0.0031

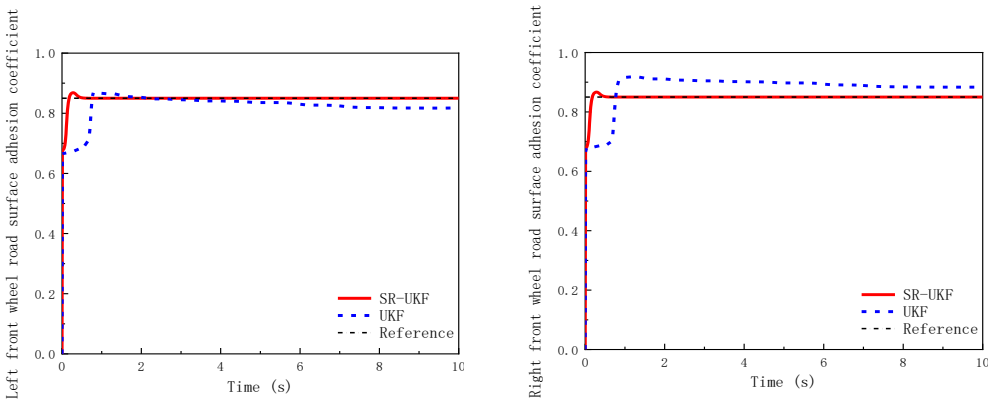

(**a**) Left front wheel

(**b**) Right front wheel

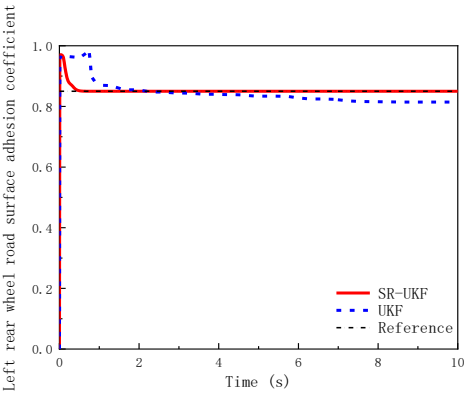

(**c**) Left rear wheel

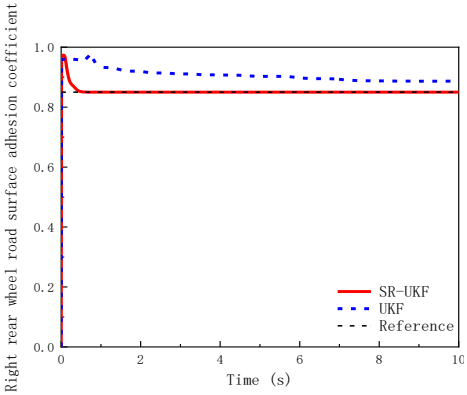

(**d**) Right rear wheel

Figure 5. Simulation comparison of straight-line acceleration performance on high-adhesion coefficient pavement.

4.2.2. Simulation Validation of Low-Low-Adhesion Coefficient Road Surface Constant-Speed Rotation Conditions

During simulation, the road surface adhesion coefficient is set to 0.35. The vehicle performs a uniform-speed turning maneuver on the road surface at 40 km/h. The steering wheel angle changes from 0° to 60° within 0–0.3 s, and remains fixed at 60° after 0.4 s. The simulation results are shown in Figure 6. After the vehicle begins turning, the SR-UKF algorithm converges rapidly, within approximately 0.3 s via SVD, yielding estimates that are highly consistent with the actual values. In contrast, the traditional UKF algorithm takes about 1.2 s to converge, exhibiting a slow convergence rate and significant deviation from the actual values after convergence. As shown in Table 4, the SR-UKF estimation results exhibit minimal inter-iteration error variations with an average absolute error of 0.0011—significantly lower than the UKF's 0.0061, representing an 82% reduction in estimation error and further validating the algorithm's stability and reliability under low-adhesion conditions. This further validates the SR-UKF algorithm's stability and reliability under low-attachment conditions.

Table 4. Mean absolute error for straight-line acceleration on low-adhesion coefficient Pavement.

Wheel	UKF	SR-UKF
Left front wheel	0.0053	0.0007
Right front wheel	0.0060	0.0009
Left rear wheel	0.0062	0.0013
Rear right wheel	0.0070	0.0013
Average value	0.0061	0.0011

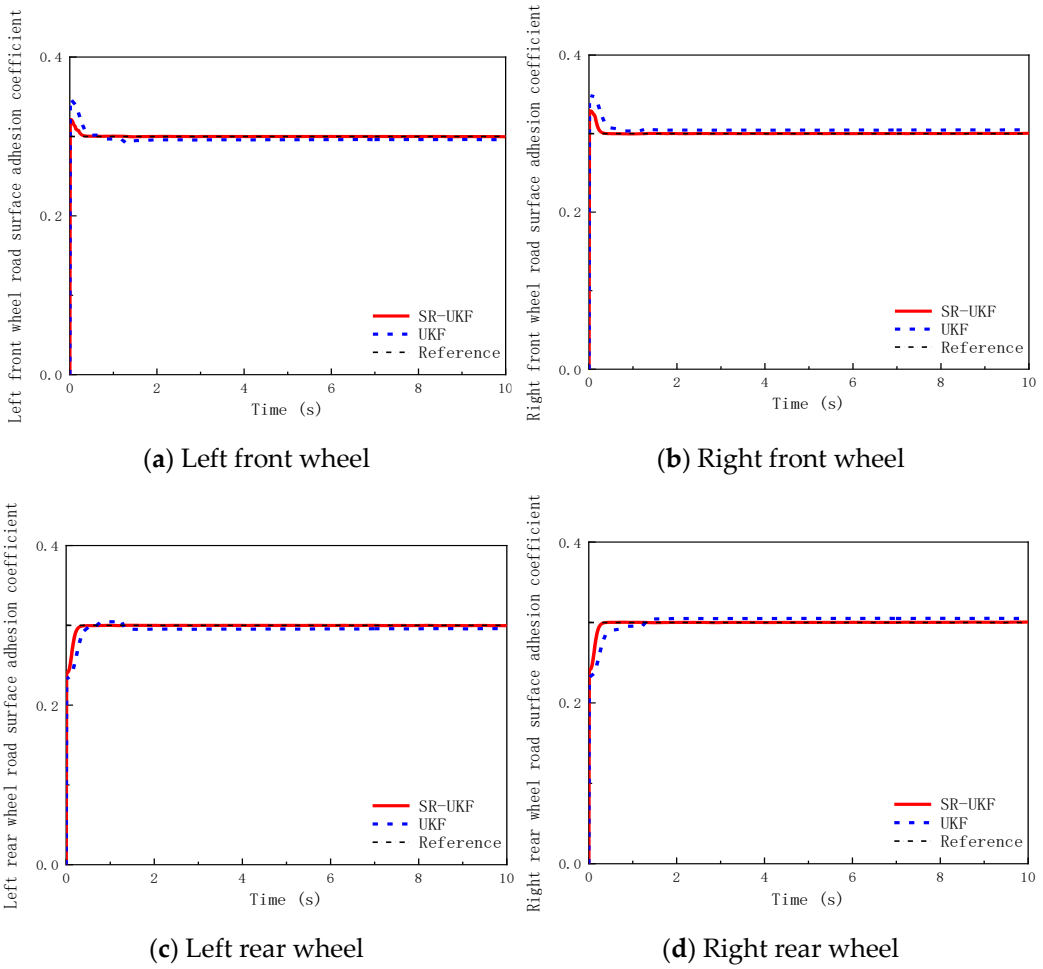

(**a**) Left front wheel (**b**) Right front wheel

(**c**) Left rear wheel (**d**) Right rear wheel

Figure 6. Simulation comparison of constant-speed rotation on low-adhesion coefficient pavement.

4.2.3. Simulation and Validation of the Straight-Line Driving at Constant Speed on a Split-μ Road Scenario

During the simulation, the left road surface adhesion coefficient was set to 0.3 and the right to 0.85. The vehicle traveled in a straight line at 40 km/h with the steering wheel at a 0° angle. The simulation results are shown in Figure 7. The SR-UKF algorithm quickly converged the estimated values of the left and right wheels to their actual values with high accuracy. In contrast, the UKF algorithm showed significant fluctuations in its estimated curves and failed to maintain stable tracking of the actual values over time. As shown in Table 5, the mean absolute error of the SR-UKF (0.0037) is much lower than that of the UKF (0.0924), indicating an estimated reduction in error of about 96%. This clearly demonstrates its superior adaptability under open-road conditions.

Table 5. Mean absolute error for straight-line driving at constant speed on a split-μ road scenario.

Wheel	UKF	SR-UKF
Left front wheel	0.0780	0.0029
Right front wheel	0.1054	0.0044
Left rear wheel	0.0781	0.0030
Rear right wheel	0.1082	0.0045
Average value	0.0924	0.0037

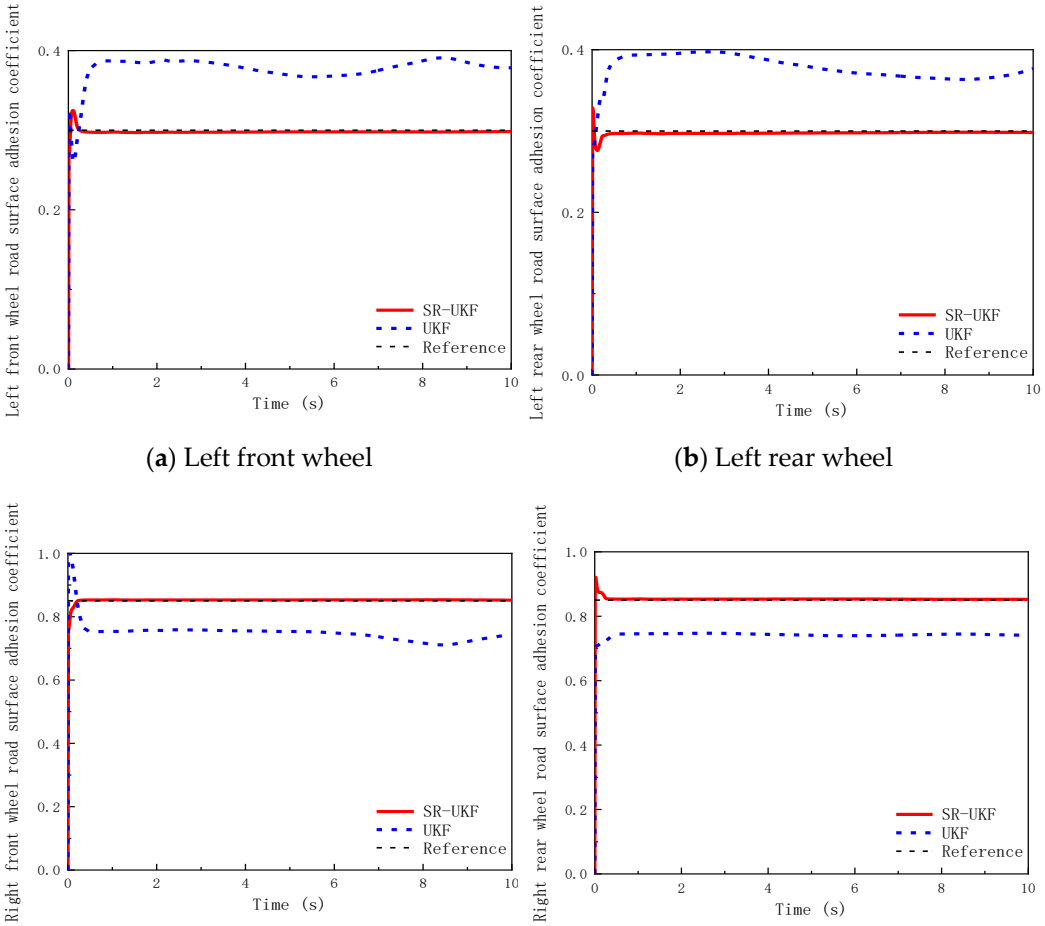

(**a**) Left front wheel (**b**) Left rear wheel

(**c**) Right front wheel (**d**) Right rear wheel

Figure 7. Simulation comparison of straight-line driving at constant speed on a split-μ road scenario.

4.2.4. Simulation Verification of Straight-Line Acceleration on Opposing-μ Road Surfaces

During simulation, set the road surface adhesion coefficient to 0.85 for the first 4 s and 0.5 for the following 6 s. The vehicle's initial speed is 20 km/h, the throttle opening is 0.3, and the steering wheel angle is 0°. As shown in Figure 8, after two switches in operating conditions, the SR-UKF quickly converged to the new actual value within approximately 0.2 s. In contrast, the UKF not only converged more slowly but also showed severe oscillations at the switching points, failing to maintain stable tracking. This demonstrates that the SR-UKF provides better suppression of system disturbances and improved robustness. As shown in Table 6, the SR-UKF achieves an average absolute error of only 0.0059, a reduction of roughly 97% compared to the UKF's 0.1922. This performance greatly surpasses that of traditional methods.

Table 6. Mean absolute error of the straight-line acceleration scenario on the opposing-μ road.

Wheel	UKF	SR-UKF
Left front wheel	0.1512	0.0061
Right front wheel	0.2125	0.0061
Left rear wheel	0.1687	0.0057
Rear right wheel	0.2363	0.0057
Average value	0.1922	0.0059

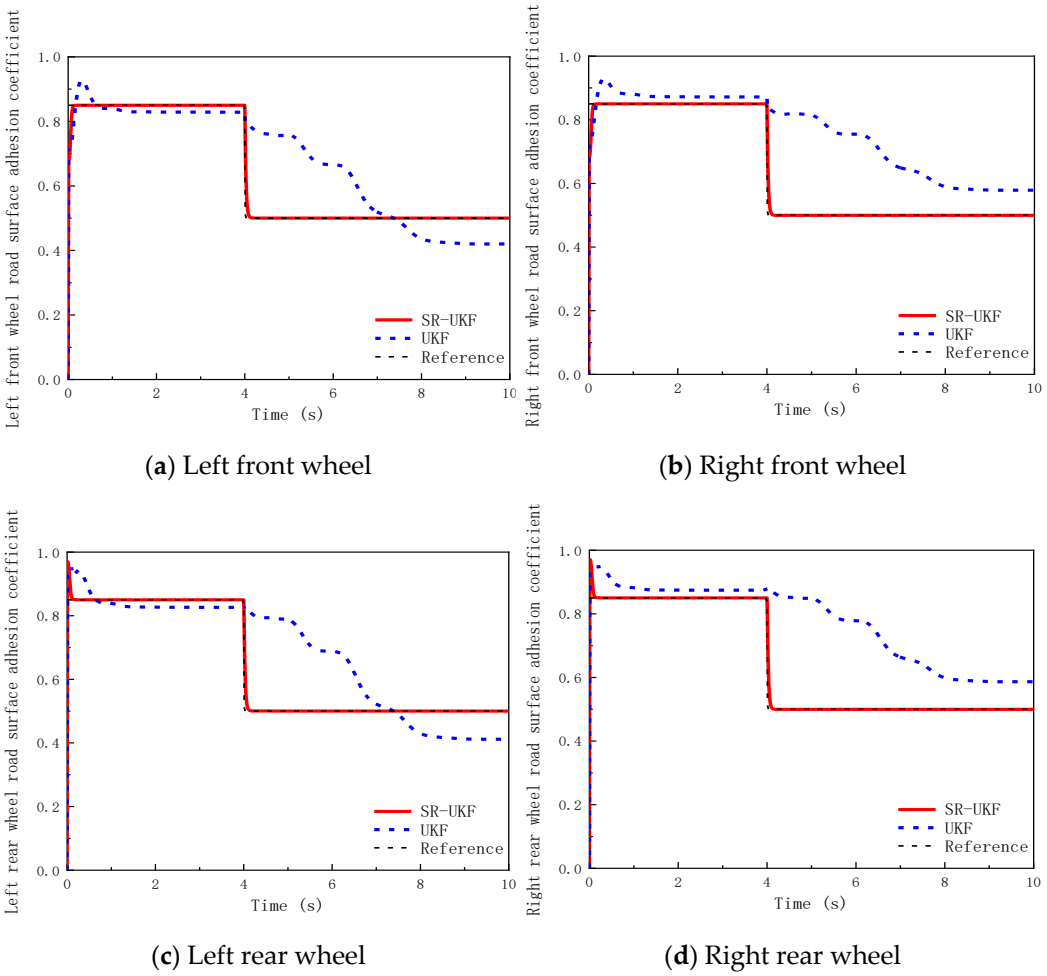

(**a**) Left front wheel (**b**) Right front wheel

(**c**) Left rear wheel (**d**) Right rear wheel

Figure 8. Simulation comparison of the straight-line acceleration scenario on the opposing-μ road.

4.3. Analysis of the Mean Absolute Error Data for Each Wheel Under Multiple Low Road Surface Adhesion Coefficients

Low-coefficient-of-adhesion road surfaces are typical conditions that cause vehicle dynamic instability, with tire–road interactions showing clear nonlinearity. To systematically explore these effects, this study simulated multiple low-adhesion surfaces with coefficients of 0.2, 0.25, 0.3, 0.35, 0.4, and 0.45. During the simulation, the vehicle traveled at a steady 40 km/h in a straight line, with the steering wheel fixed at 0°. As shown in Figure 9, the mean absolute error (MAE) for the left front wheel, right front wheel, left rear wheel, and right rear wheel stays low under these low-adhesion conditions. The parameters in Table 7 show small error fluctuations for each wheel, indicating that this algorithm provides high accuracy and robustness in estimating the four-wheel system on low-adhesion road surfaces.

Table 7. Average absolute error for each wheel under various low road surface adhesion coefficients.

Road Surface Adhesion Coefficient	Left Front Wheel MAE	Right Front Wheel MAE	Left Rear Wheel MAE	Right Rear Wheel MAE
0.2	0.00048	0.00052	0.00056	0.00061
0.25	0.00042	0.00044	0.00048	0.00051
0.3	0.00047	0.00048	0.00049	0.00053
0.35	0.00060	0.00064	0.00059	0.00063
0.4	0.00079	0.00076	0.00089	0.00083
0.45	0.00085	0.00080	0.00089	0.00089

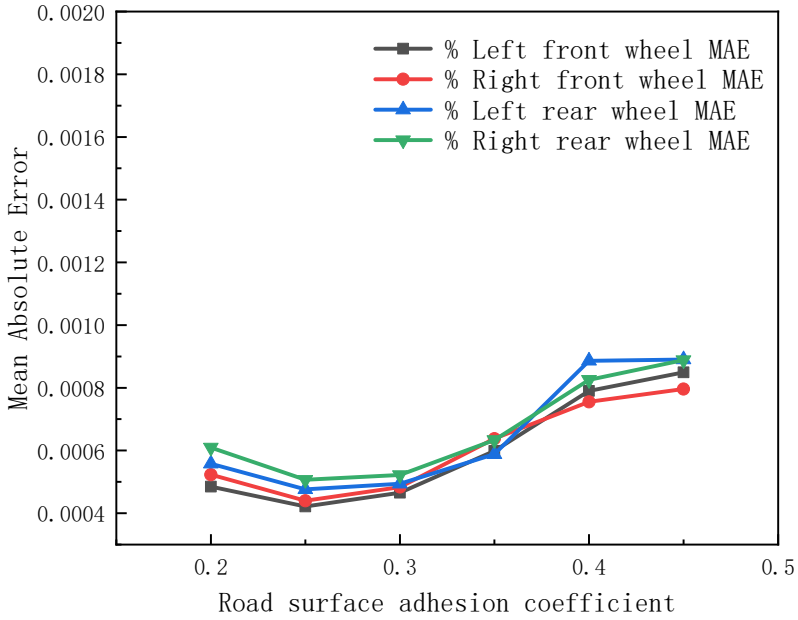

Figure 9. Analysis of the mean absolute error data for each wheel under multiple low road surface adhesion coefficients.

5. Conclusions

To address the need for estimating road surface friction coefficients in distributed-drive electric vehicles, a friction coefficient estimation method based on the SR-UKF is proposed and validated through simulation tests under various operating conditions.

1. A nonlinear seven-degree-of-freedom vehicle model was developed based on the Dugoff-modified tire model, using the Carsim/Simulink co-simulation platform to create a distributed drive electric vehicle simulation model. It incorporates a speed-tracking model that provides a basis for estimating road adhesion coefficients.
2. Building on the traditional UKF algorithm, the SR-UKF algorithm is developed by applying root-mean-square covariance processing and incorporating SVD. This algorithm consistently maintains matrix positivity to ensure numerical stability while speeding up convergence. It fully utilizes measurement data to estimate target values accurately.
3. To thoroughly assess the algorithm's performance, this study conducted simulation validation across various common road conditions, including high-friction, low-friction, and dual-surface roads. Results show that, compared to the traditional UKF, the proposed SR-UKF algorithm converges faster and provides significantly improved estimation accuracy. Particularly on low-friction surfaces, an in-depth analysis of the mean absolute error across all wheels further confirms the SR-UKF's superiority in estimation precision and robustness.

Author Contributions: Conceptualization, J.L. and X.W.; formal analysis, X.W.; methodology, X.W.; software, X.W.; validation, X.W.; visualization, H.P.; writing—original draft, X.W.; writing—review and editing, J.L. All authors have read and agreed to the published version of the manuscript.

Funding: This work was supported by the school–enterprise cooperation project (Grant No. heng20250110).

Data Availability Statement: The data are part of an ongoing study, so it is not currently convenient to publish the code and data. However, we welcome other researchers discussing this with us.

Conflicts of Interest: Author Hui Peng was employed by Henan Urban Transportation Planning and Design Institute Co., Ltd. The remaining authors declare that the research was conducted in the

absence of any commercial or financial relationships that could be construed as a potential conflict of interest.

References

1. Zhang, H.; Hua, W. Review of Hub Motors and Related Technologies for Distributed Drive Systems. *Trans. Chin. Soc. Electr. Eng.* **2024**, *44*, 2871–2886. [CrossRef]
2. Alsaleh, A. Hybrid Deep Learning Approach for Secure Electric Vehicle Communications in Smart Urban Mobility. *Vehicles* **2025**, *7*, 112. [CrossRef]
3. Wang, S.; Zhang, H.; Zhao, X.; Zheng, Z.; Song, H.; Guo, H. Research on lateral stability control strategy for distributed drive electric vehicles considering driving style. *J. Frankl. Inst.* **2024**, *361*, 106921. [CrossRef]
4. Song, Q.; Wang, G.; Shang, H.; Zhang, N. Research on a Multi-Parameter Control-Based Manoeuvring Stability Control Strategy for Distributed-Drive Electric Vehicles. *Automot. Eng.* **2023**, *45*, 2104–2112+2138. [CrossRef]
5. Li, H.; Jin, L.; Li, J.; Xiao, F.; Wang, Z.; Zhang, G. Braking Force Coordination Control for In-Wheel Motor Drive Electric Vehicles with Electro-Hydraulic Composite Braking System. *Vehicles* **2025**, *7*, 119. [CrossRef]
6. Pusztai, Z.; Luspay, T.G.; Friedler, F. LTV-LQG Control for an Energy Efficient Electric Vehicle. *Vehicles* **2025**, *7*, 113. [CrossRef]
7. Shoman, M.; Cerezo, V. Modeling and Simulation of an Electric Rail System: Impacts on Vehicle Dynamics and Stability. *Vehicles* **2025**, *7*, 36. [CrossRef]
8. Stefanelli, R.; Fichera, G.; Genovese, A.; Dell'Annunziata, G.N.; Sakhnevych, A.; Timpone, F.; Farroni, F. A Comprehensive Review of Rubber Contact Mechanics and Friction Theories. *Appl. Sci.* **2025**, *15*, 11558. [CrossRef]
9. Sun, H.; Wang, H. Research on Electric Vehicle Differential System Based on Vehicle State Parameter Estimation. *Vehicles* **2025**, *7*, 80. [CrossRef]
10. Yuan, C.; Zhang, L.; Chen, L. Review and Outlook on the Development of Road Surface Friction Coefficient Identification Methods. *Mech. Manuf. Autom.* **2018**, *47*, 1–4+7. [CrossRef]
11. Zhang, L.; Guan, K.; Ding, X.; Guo, P.; Wang, Z.; Sun, F. A Method for Estimating Road Surface Friction Coefficient Based on Image Recognition and Kinematic Fusion. *Automot. Eng.* **2023**, *45*, 1222–1234+1262. [CrossRef]
12. Xu, W. Image Road Detection and Recognition Algorithms Based on Machine Vision. *Lect. Notes Electr. Eng.* **2025**, *1355*, 449–456. [CrossRef]
13. Chen, J.; Huang, X.; Zheng, B.; Zhao, R.; Liu, X.; Cao, Q.; Zhu, S. Real-time identification system of asphalt pavement texture based on the close-range photogrammetry. *Constr. Build. Mater.* **2019**, *226*, 910–919. [CrossRef]
14. Xu, Z.; Wang, J.; Lu, Y.; Li, H. Estimation Strategy for the Adhesion Coefficient of Arbitrary Pavements Based on an Optimal Adaptive Fusion Algorithm. *Machines* **2024**, *13*, 17. [CrossRef]
15. Huang, J.; Chen, X.; Jin, Q.; Li, P. A Fusion Estimation Method for Tire-Road Friction Coefficient Based on Weather and Road Images. *Lubricants* **2025**, *13*, 459. [CrossRef]
16. Deng, H.; Zhao, Z.; Zhao, K.; Li, G.; Yu, Q. Estimation of Road Adhesion Coefficient Using Interactive Multiple Model Adaptive Unscented Kalman Filter for 4WID Vehicles. *Qiche Gongcheng/Automot. Eng.* **2024**, *46*, 1357–1369. [CrossRef]
17. Ge, P.; Zhang, C.; Zhang, T.; Guo, L.; Xiang, Q. Maximum Correntropy Square-Root Cubature Kalman Filter with State Estimation for Distributed Drive Electric Vehicles. *Appl. Sci.* **2023**, *13*, 8762. [CrossRef]
18. Wang, H.; Wang, C.; Gao, H.; Xu, S. Vehicle traction force control based on the road adhesion coefficient estimation by FFUKF. *Chin. J. Theor. Appl. Mech.* **2022**, *54*, 1866–1879. [CrossRef]
19. Yang, X.; Zheng, L.; Jin, Y.; Zhang, H.; Zeng, D.; Ji, J. Fusion Estimation Method of Tire-road Friction Coefficient Based on Vehicle Vision and Dynamical Model. *J. Mech. Eng.* **2024**, *60*, 254–264. [CrossRef]
20. Liu, Z.Q.; Liu, Y.Q. Adaptive Kalman filter estimation of road surface friction coefficients. *J. Highw. Eng.* **2020**, *33*, 176–185. [CrossRef]
21. Zhang, R.; Feng, Y.; Shi, P.; Zhang, B.; Liu, Y. Estimation of Road Surface Friction Coefficient for Distributed Electric Vehicles. *Mach. Sci. Technol.* **2025**, *44*, 187–198. [CrossRef]
22. Chen, Z.; Li, G.; Zhang, Z.; Fan, R. Joint Estimation of Driving State and Road Surface Adhesion Coefficient of a Four-Wheel Independent and Steering-Drive Electric Vehicle. *World Electr. Veh. J.* **2024**, *15*, 249. [CrossRef]
23. Useros, M.M.; Monasterio, F.V.; Salas, M.J.; Boada, M.J.L. Static Output-Feedback Path-Tracking Controller Tolerant to Steering Actuator Faults for Distributed Driven Electric Vehicles. *World Electr. Veh. J.* **2025**, *16*, 40. [CrossRef]
24. Guo, J.; Dai, Z.; Liu, M.; Xie, Z.; Jiang, Y.; Yang, H.; Xie, D. Distributed Drive Electric Vehicle Handling Stability Coordination Control Framework Based on Adaptive Model Predictive Control. *Sensors* **2024**, *24*, 4811. [CrossRef]
25. Tian, Y.T.; Zhang, Y.; Wang, X.Y.; Chen, H. Estimation of Centre of Gravity Yaw Angle in Electric Vehicles Based on Square-Root Trace-Free Kalman Filtering Algorithm. *J. Jilin Univ. (Eng. Sci.)* **2018**, *48*, 845–852. [CrossRef]
26. Cheng, J.; Yang, K.; Hu, X. Research on SOC Estimation of Lithium-Ion Battery Based on CA-SVDUKF Algorithm. *Batteries* **2025**, *11*, 435. [CrossRef]

27. Liu, S.; Guo, Y. Vehicle Pose Estimation Method Based on Maximum Correntropy Square Root Unscented Kalman Filter. *Appl. Sci.* **2025**, *15*, 5662. [CrossRef]
28. Wan, W.; Feng, J.; Song, B.; Li, X. Huber-Based Robust Unscented Kalman Filter Distributed Drive Electric Vehicle State Observation. *Energies* **2021**, *14*, 750. [CrossRef]
29. Wang, X.; Dong, Z.; Wang, S.; Ji, F.; Zou, B. Wide-temperature multi-condition SOC estimation for lithium-ion batteries based on an improved open-circuit voltage model and adaptive square-root unscented Kalman filter. *J. Electr. Eng.* **2024**, *39*, 7950–7964. [CrossRef]
30. Li, T. Research on Tire-Road Surface Friction Coefficient Identification Algorithm Based on EPS Torque Information. Master's Thesis, China University of Geosciences, Beijing, China, 2016. [CrossRef]
31. Allam, A.; Mangold, M.; Zhang, P. Square Root Unscented Kalman Filter-Based Multiple-Model Fault Diagnosis of PEM Fuel Cells. *Sensors* **2025**, *25*, 29. [CrossRef] [PubMed]

Disclaimer/Publisher's Note: The statements, opinions and data contained in all publications are solely those of the individual author(s) and contributor(s) and not of MDPI and/or the editor(s). MDPI and/or the editor(s) disclaim responsibility for any injury to people or property resulting from any ideas, methods, instructions or products referred to in the content.